

RESEARCH

Open Access



Boosting immunogenic cell death via hollow MnO₂-based multiple stimuli-responsive drug delivery systems for improved cancer immunotherapy

Yueyao Wu^{1,2†}, Runtian Wang^{1†}, Peiliang Shen², Weijia Zhou², Chao Chen², Kaiyong Yang², Jingjing Yang^{2,3}, Yujun Song^{3*}, Xin Han^{1,2*} and Xiaoxiang Guan^{1,4*}

[†]Yueyao Wu and Runtian Wang have contributed equally to this work

*Correspondence: ysong@nju.edu.cn; xhan0220@njucm.edu.cn; xguan@njmu.edu.cn

¹Department of Oncology, The First Affiliated Hospital of Nanjing Medical University, Nanjing 210029, China

²Jiangsu Key Laboratory for Pharmacology and Safety Evaluation of Chinese Materia Medica, School of Medicine and Holistic Integrative Medicine, Nanjing University of Chinese Medicine, Nanjing 210023, China

³College of Engineering and Applied Sciences, State Key Laboratory of Analytical Chemistry for Life Science, Nanjing University, Nanjing 210023, China

⁴Jiangsu Key Lab of Cancer Biomarkers, Prevention and Treatment, Collaborative Innovation Center for Personalized Cancer Medicine, Nanjing Medical University, Nanjing 211166, China

Abstract

Cancer treatment by inducing tumor cell immunogenic cell death (ICD) is critical for tumor therapy. However, ICD activation by single pathway is often limited in practical application due to its low efficiency. In addition, the low pH and anoxic microenvironments in solid tumors greatly limit the effective activation of ICD. Herein, hollow manganese dioxide (H-MnO₂) nanomaterials were selected to load both Mitoxantrone (MTZ) and Chlorin e6 (Ce6) due to its hollow structure and ability to release drugs in the acidic environments. Thus, the synergy of photodynamic therapy (PDT), photothermal therapy (PTT) and chemotherapy can induce the process of immunogenic cell death, stimulate the maturation of dendritic cells (DCs), and activate the immune response to kill tumor cells dramatically. Efficient immunotherapeutic effects were obtained when MnO₂-C/M-HA was given intravenously to 4T1 tumor-bearing BALB/c mice with 660 nm near-infrared laser irradiation. This study overcame the limitations of monotherapy and provided a multifunctional platform for tumor immunotherapy.

Keywords: Manganese dioxide, Photodynamic therapy, Photothermal therapy, Chemotherapy, Immunogenic cell death

Introduction

Immunotherapy for cancer usually includes immune checkpoint therapy, CAR-T cell technology, and cancer vaccines (Yang 2015; Zhang and Zhang 2020). The immunogenicity of tumor cells is an emerging determinant of tumor immunotherapy. It has been found that it is possible to increase the immunogenicity of tumor cells by modulating their death process (Garg and Agostinis 2017). Immunogenic cell death (ICD) is a process in which dying tumor cells promote the maturation of dendritic cells by producing damage associated molecular patterns (DAMPs), including calreticulin (CRT), high-mobility group box 1 (HMGB1), and adenosine triphosphate (ATP) (Krysko et al. 2012; Kroemer et al. 2013). Mature dendritic cells can present antigens to T cells and promote



the formation of cytotoxic CD8⁺ T lymphocytes (Bol et al. 2016; Sabado et al. 2017), thus further realizing the killing of tumor cells.

ICD can usually be induced by some phototherapeutic pathways. Photodynamic therapy (PDT) mainly refers to a process in which the photosensitizer is activated by laser irradiation with specific wavelength and reactive oxygen species (ROS) are produced, thus producing cytotoxic effects on tumor cells (Agostinis et al. 2011; Donohoe et al. 2019). The PDT process has been reported to be able to induce ICD (Alzeibak et al. 2021). While photothermal therapy (PTT) is that, after laser irradiation photothermal agent produces high temperature above 42 °C, thus inducing the damage and necrosis of tumor cells (Zou et al. 2016; Deng et al. 2021). PTT is also a pathway to induce ICD (Xu and Liang 2020). What's more, some common chemotherapeutic drugs such as doxorubicin (DOX) (Dai et al. 2020), can also be used as inducers of ICD. However, the use of a kind of single treatment to induce ICD-induced treatment is not strong. For instance, phototherapy approaches such as PDT and PTT are often inefficient in their anti-tumor treatment due to the limited tissue penetration during laser irradiation (Jeong et al. 2021). In particular, the PDT process is extremely oxygen-dependent. Therefore, combining multiple therapeutic approaches such as PDT, PTT and chemotherapy may induce higher levels of ICD to increase tumor immunogenicity (Li et al. 2019; Zhang et al. 2021).

Mitoxantrone (MTZ) as a chemotherapy agent can induce ICD (Fan et al. 2017; Mei et al. 2020). In addition, it can also be used as a photothermal agent due to its strong near-infrared absorption in the wavelength range of 600–700 nm (Wang et al. 2020a, b; Ni et al. 2021). Chlorin e6 (Ce6), a common photosensitizer, can be activated by near-infrared laser at 660 nm to induce the production of ROS (Phua et al. 2019; Wang et al. 2020a, b). Thus, Ce6 should be a good option to use in conjunction with MTZ. But the PDT process depends on the abundance of oxygen (O₂), so it is often limited by the tumor's anoxic environment to produce enough ROS (Sun et al. 2020). Moreover, free MTZ and Ce6 have limited targeting and are difficult to reach the tumor site. Hence, we need to find a suitable carrier to simultaneously load two drugs and assist them to achieve better synergistic therapy.

Tumor tissue is usually in a low pH, anoxic environment (Boedtkjer and Pedersen 2020; Liu et al. 2021a, b). Its unique properties can greatly limit the function of cytotoxic T lymphocytes, while manganese dioxide (MnO₂) can react with glutathione (GSH) or hydrogen peroxide (H₂O₂) in acidic tumor microenvironment to decompose into Mn²⁺ and produce O₂ to improve the hypoxic tumor environment (Yang et al. 2017; Cao et al. 2020; Huang et al. 2020). The O₂ produced during this reaction can be used by the PDT process. Besides, hollow MnO₂ structure can also achieve effective drug delivery and drug release (Yang et al. 2017), which can be used as an efficient drug delivery carrier.

In this work, we synthesized MnO₂-C/M-HA nanomaterials to implement the photochemo-immunotherapy (Fig. 1). The hollow MnO₂ structure was used to load the photothermal chemotherapy agent MTZ and the photosensitizer Ce6. The outer layer was coated with hyaluronic acid (HA). After entering the acidic environment of tumor, MnO₂ could react with GSH and H₂O₂, degrade to Mn²⁺, and then the two drugs were released. The nanomaterials could produce enough O₂ by reacting with H₂O₂. Under 660 nm near-infrared light stimulation, the activation of Ce6 induced the production

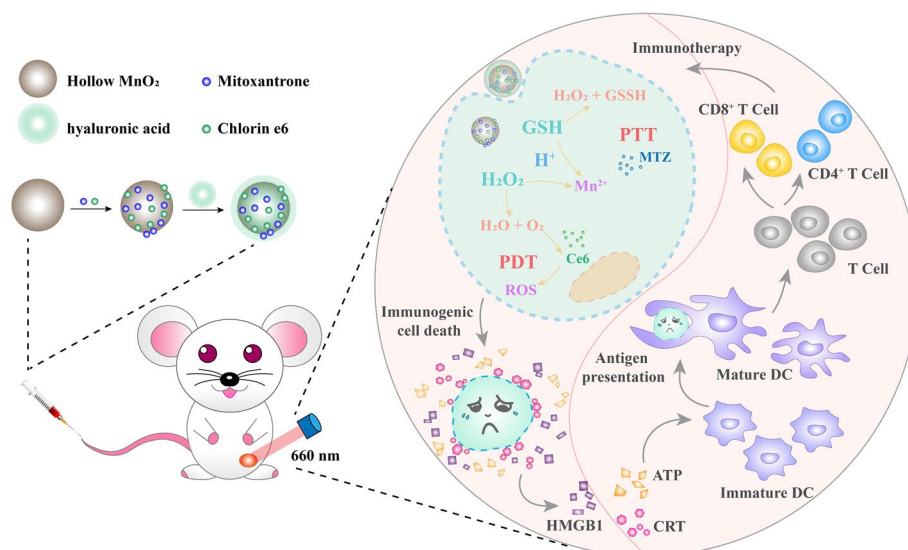


Fig. 1 Schematic illustration of designing MnO₂-C/M-HA for photo-chemo-immunotherapy. MnO₂ degrades after reaction in acidic environment, releasing Ce6 and MTZ. Under the irradiation of 660 nm near-infrared laser, Ce6 is activated and induces ROS production. MTZ also plays a role in both chemotherapy and PTT. Synergistically stimulate tumor cells to release DAMPs, promote DCs maturation, and further induce anti-tumor immune response

of ROS, resulting in toxic effects on tumor cells. Meanwhile, MTZ also induced thermal ablation of tumor cells by photothermal heating. The chemotherapy effect of MTZ itself, combined with PDT and PTT, could induce strong ICD effects. DAMPs release from dying tumor cells were stimulated to induce DCs maturation, which could present antigens to T cells and activate anti-tumor immunity.

Materials and methods

Materials, cell lines and animals

Ammonium hydroxide, formaldehyde (HCHO) and potassium permanganate (KMnO₄) were purchased from TCI (Shanghai, China). Tetraethyl orthosilicate (TEOS) and resorcinol were purchased from Aladdin (Shanghai, China). Chlorin e6 (Ce6) was purchased from Meilunbio (Dalian, China). Mitoxantrone (MTZ) was purchased from MedChemExpress (Shanghai, China). hyaluronic acid (HA) was purchased from Feiyubio (Nantong, China). 4',6-diamidino-2-phenylindole (DAPI), 2',7'-dichlorodihydrofluorescein diacetate (DCFH-DA), calcein/propidium iodide (PI) Cell Viability/Cytotoxicity Assay Kit and ATP Assay Kit were purchased from Beyotime (Shanghai, China). Cobalt chloride (CoCl₂) was purchased from TMstandard (Beijing, China). MTS Cell Proliferation and Cytotoxicity Assay Kit was purchased from Keygenbio (Nanjing, China). YF[®]488-Annexin V/PI Cell Apoptosis Kit was purchased from Bioscience (Shanghai, China). GM-CSF and Recombinant Mouse IL-4 were purchased from Novoprotein (Beijing, China). Collagenase I and Collagenase IV were purchased from BioFroxx (Germany). HMGB1 ELISA kit was purchased from MSKBIO (Wuhan, China). Mouse TNF- α and IL-6 Precoated ELISA kit were purchased from DAKWE (Beijing, China). Antibodies used in this study are listed in Additional file 1: Table S1. 4T1 cells were purchased from American Type Culture Collection and incubated under 37 °C within 5%

CO₂ atmosphere. Culture medium was composed of high-glucose Dulbecco's modified Eagle's medium (DMEM), 10% fetal bovine serum (FBS), 1% penicillin and streptomycin. BALB/c female mice (SPF grade, 4–6 weeks old, weighing approximately 18 g) were purchased from Huachuang Sino (202203A002). These mice were raised in Laboratory Animal Center of Nanjing University of Chinese Medicine. All experiments conformed to animal ethics.

Synthesis of MnO₂-C/M-HA

The H-MnO₂ were synthesized by a previously reported method (Yang et al. 2017). Firstly, 1.3 mL ammonium hydroxide and 1.4 mL TEOS were added to a 2:1 mixture of ethanol and distilled water. The white translucent SiO₂ core was obtained by water bath stirring at 30 °C. Then, 0.12 g resorcinol and 0.3 mL HCHO were added and mixed overnight at 30 °C to obtain the SiO₂@RF template. After centrifugation at 12,000 rpm and cleaning for three times, 0.4 g KMnO₄ was added for ultrasonic reaction for 6 h. After centrifugation at 12,000 rpm and cleaning for three times, precipitation was taken and resuspended. Then an appropriate amount of 1 M NaOH solution was added, and etched in water bath at 80 °C for 6 h. After centrifugation at 12,000 rpm and cleaning for three times, H-MnO₂ products could be obtained. For drug loading, the H-MnO₂ solution (1.0 mg mL⁻¹) was mixed with different concentrations of Ce6 and MTZ for 12 h at room temperature. Before that, the stock solution of the drug was diluted with pure water to the required concentration before loading. Finally, the loaded product was mixed with 0.5 mg mL⁻¹ HA whose pH had been adjusted to 7.4 for 2 h under the normal temperature. After centrifugation at 12,000 rpm and cleaning for three times, MnO₂-C/M-HA could be obtained.

Characterizations

Transmission electron microscopy (TEM, JEM-2200CX) was applied to characterize the morphology of nanomaterials. UV–vis spectra were measured by multiskan spectrum (FlexA-200). The zeta potentials of nanomaterials were determined by a zeta potential analyzer (NanoSight NS300). The nitrogen adsorption curve was measured by specific surface and porosity analyzer (ASAP 2460 3.01). The supernatant was detected by spectrophotometry (NanoDrop 2000C) for drug loading and release.

Photothermal properties and stability

Various concentrations of MnO₂-C/M-HA solutions (20, 40, 60, 80 and 100 µg mL⁻¹) were irradiated by 660 nm laser (1.0 W cm⁻², 15 min). The changes in temperature were monitored by the infrared camera (Testo 869). Then, 660-nm laser with different power densities (0.6, 0.7, 0.8, 0.9 and 1.0 W cm⁻²) were applied to 100 µg mL⁻¹ MnO₂-C/M-HA solutions and the temperature was recorded. Next, H₂O, Ce6 and H-MnO₂ were also measured as comparisons. At last, the temperature in the heating–cooling process and four cycles of on/off states were also measured.

Cellular uptake

4T1 cells were seeded in 24-well plates for 24 h. Then, the medium in each well was replaced with the same concentration (20 µg mL⁻¹) of free Ce6 or MnO₂-Ce6-HA for 2 h

or 6 h. Wash with PBS three times to remove unswallowed drugs. After fixation with 4% paraformaldehyde for 15 min, the cells were labeled with 4',6-diamidino-2-phenylindole (DAPI). Wash three times with PBS to remove excess DAPI. The samples were imaged by cellular imaging system (Thunder, Leica).

Cell viability and cytotoxicity assay

For cell cytotoxicity assay, 4T1 cells were seeded in 96-well plates at a density of 5×10^3 per well for 24 h. Therein, CoCl_2 was utilized to mimic hypoxia in 4T1 breast cancer cells (Yu et al. 2021). 4T1 cells were seeded in 96-well plates overnight and then pretreated with PBS containing 100 μM CoCl_2 for 8 h. Then, 4T1 cells were incubated with PBS, MnO_2 -HA, MnO_2 -Ce6-HA, MnO_2 -MTZ-HA and MnO_2 -C/M-HA for 6 h and then treated with or without 660 nm laser irradiation (1.0 W cm^{-2} , 15 min). For another 24 h, the cell viability was studied by MTS assay and the absorbance at 490 nm was measured by a multiskan spectrum (FlexA-200). To further compare cell activity and cytotoxicity between different treatment groups, calcein-AM and propidium iodide (PI) double-fluorescent staining were used for cell live/dead assay. In addition, YF[®]488-Annexin V and PI were also used to dye cells for flow cytometric analysis to calculate the apoptosis rate of the cells.

Detection of cellular ROS

4T1 cells were seeded in 24-well plates for 24 h under normoxic and hypoxic conditions. Then, 4T1 cells were incubated with PBS, Ce6, MnO_2 -Ce6-HA and MnO_2 -C/M-HA for 6 h and then treated with or without 660 nm laser irradiation (1.0 W cm^{-2} , 15 min). After changing serum-free medium, the 2',7'-dichlorodihydrofluorescein diacetate (DCFH-DA) was added to each well for 20 min (Han et al. 2020; Wang et al. 2020a, b). After washing with PBS for three times, the samples were observed under a fluorescence microscope (MF52-N).

In vitro detection of ICD biomarkers

For the western blot detection of CRT and HMGB1, 4T1 cells (2×10^5 per well) were seeded in 6-well plate. Then, the cells were incubated with PBS, MTZ, MnO_2 -MTZ-HA and MnO_2 -C/M-HA for 6 h, and irradiated with or without 660 nm laser irradiation (1.0 W cm^{-2} , 15 min). Following another 24 h, the supernatant of cell culture medium was collected for enzyme-linked immunosorbent assay (ELISA) and the extraction of cell protein was carried out for subsequent operations. After electrophoresis, membrane transfer, blocking, primary antibody incubation and secondary antibody incubation, the final samples were developed with imaging system (Azure C-500). For the immunofluorescence (IF) of CRT and HMGB1, 4T1 cells (5×10^4 per well) were seeded in 24-well plate containing cellular slivers. Then, the cells were incubated with PBS, MTZ, MnO_2 -MTZ-HA and MnO_2 -C/M-HA for 6 h, and irradiated with or without 660 nm laser irradiation (1.0 W cm^{-2} , 15 min). Following another 24 h, the cells on slivers were fixed for subsequent operations. After the process of fixation, permeabilization, blocking and immunostaining, counter staining and mounting, the final samples were imaged by cellular imaging system (Thunder, Leica). Calreticulin-Rabbit Polyclonal Antibody and HMGB1-Rabbit Polyclonal Antibody were used for primary antibodies. Secondary

antibody for western blot was Goat anti-Rabbit IgG. Secondary antibody for IF was CoraLite 488 or Cy3-Goat anti-Rabbit IgG.

Detection of intracellular ATP

4T1 cells (1×10^5 per well) were seeded in 12-well plate and then incubated with PBS, MTZ, MnO_2 -MTZ-HA and MnO_2 -C/M-HA for 6 h, and irradiated with 660 nm laser irradiation (1.0 W cm^{-2} , 15 min). For another 24 h, remove the medium and add 100 μl cell lysate per well. After centrifugation at 12,000 g at 4°C for 5 min, supernatant was taken for subsequent determination.

In vitro DC maturation

Bone marrow-derived dendritic cells (BMDCs) were obtained from BALB/c female mice femur and tibia, then cultured in DMEM medium supplemented with 15% FBS, GM-CSF (20 ng mL^{-1}) and IL-4 (10 ng mL^{-1}) at 37°C for 6 days to acquire immature DC. Then, 4T1 cells and BMDCs were inoculated on both sides of non-contact communication cell chip for 24 h. Next, 4T1 cells were incubated with PBS and MnO_2 -C/M-HA for 6 h, and irradiated with 660 nm laser irradiation (1.0 W cm^{-2} , 30 min). For another 24 h, the cells were fixed for immunofluorescence staining. PE/Cyanine7 anti-mouse CD11c, APC anti-mouse CD80 and PE anti-mouse CD86 were used for staining.

Ex vivo fluorescence imaging and in vivo photothermal effect

For ex vivo imaging, the 4T1 tumor-bearing mice were intravenously injected with free Ce6 or MnO_2 -C/M-HA, and the mice were killed at 12 h after injection, and the major organs were collected for imaging. The fluorescence images were taken by an optical imaging system (IVIS Spectrum, PerkinElmer). 4T1 tumor-bearing mice were intravenously injected with PBS and MnO_2 -C/M-HA of 2.5 mg kg^{-1} , followed by irradiated (1.0 W cm^{-2} , 660 nm) for 5 min. The changes in tumor temperature were monitored by the infrared camera (Testo 869).

In vivo synergistic anti-tumor therapy

4T1 cells (5×10^6) were subcutaneously injected into the breast pad of female BALB/c mice (4–6 weeks, 18–20 g). Then, the mice were randomly divided into 7 groups ($n=5$). When the tumor volume reached 100 mm^3 , mice were intravenously injected with PBS, Free MTZ + Ce6, MnO_2 -Ce6-HA, MnO_2 -MTZ-HA and MnO_2 -C/M-HA of 2.5 mg kg^{-1} every 3 days. At 12 h post-injection, some groups of mice were irradiated by 660 nm laser for 5 min (1.0 W cm^{-2}). Tumor volumes and body weight were measured every other day, and tumor volumes were measured by the equation: $V = (\text{length}) \times (\text{width})^2 / 2$. After 14 days of treatment, the mice were killed and the tumor, heart, liver, spleen, lung, kidney tissues and peripheral blood were collected. The fixed tumor sections were subjected to immunohistochemistry or immunofluorescence assay. The other major organ tissues were also stained with hematoxylin and eosin (H&E).

In vivo immune response of the combined therapeutics

Tumor tissue samples were lysed with RIPA lysis buffer according to the protocol and tumor tissue proteins were extracted for western blot. Tumor tissues were cut into small

pieces and immersed in 0.5 mg mL⁻¹ Collagenase I and 0.5 mg mL⁻¹ Collagenase IV solution for 40 min at 37 °C to obtain single-cell suspension. Then, the cells were stained with PE/Cyanine7 anti-mouse CD11c, APC anti-mouse CD80, Brilliant Violet 421™ anti-mouse CD86, APC anti-mouse CD3 and PE anti-mouse CD8, followed by flow cytometry analysis (Beckman Gallios). Proinflammatory cytokines in serum including TNF-α and IL-6 were detected by ELISA immunoassay kit.

Biosafety assessment of MnO₂-C/M-HA

In order to evaluate the biosafety of MnO₂-C/M-HA *in vivo*, 12 healthy female BALB/c mice were prepared. And peripheral blood was collected at day 1, 4 and 7 after tail vein injection of MnO₂-C/M-HA for biochemical analysis of liver and kidney function. Mice blood cells were collected for hemolysis experiment. The whole blood collected in the anticoagulant tube was centrifuged at 3000 rpm for 10 min to obtain blood cells. After three times cleaning with PBS, the blood cells were diluted to 4% volume concentration. Nanomaterials of different concentrations were mixed with blood cells, and the volume concentration of blood cells was 2%. After incubation at 37 °C for 3 h, the blood cells were centrifuged at 3000 rpm for 15 min, and the supernatant was taken to measure the absorbance at 540 nm. Hemolysis rate (%) = [OD (sample) – OD (PBS)]/[OD (ddH₂O) – OD (PBS)] × 100%.

Statistical analysis

All the data were presented as mean ± SD. One-way analysis of variance (ANOVA) was used to determine the significance of the difference. Statistical significance was set at **p* < 0.05, ***p* < 0.01, ****p* < 0.001.

Results and discussion

Synthesis and characterization of MnO₂-C/M-HA

The procedure for the synthesis of H-MnO₂ is illustrated in Additional file 1: Fig. S1. We first prepared SiO₂, on this basis to form SiO₂@RF and further synthesize SiO₂@MnO₂. This method mainly used SiO₂ as the core, and then formed MnO₂ shell through the chemical reaction between RF and KMnO₄. Finally, the SiO₂@MnO₂ can be etched into H-MnO₂ under alkaline conditions. The H-MnO₂ presented mesoporous shell and hollow spherical structure which observed by transmission electron microscopy (TEM) (Fig. 2a). The porosity and specific surface of H-MnO₂ were measured by Brunauer–Emmett–Teller (BET). Nitrogen adsorption experiments showed that H-MnO₂ had a high specific surface area due to its hollow structure and pores, which proved that H-MnO₂ could be used as an effective drug delivery carrier (Fig. 2b). MTZ is a commonly available chemotherapy drug for delivery. Ce6 is also a commonly used photosensitizer. The two drugs diluted into different concentrations were mixed with 1 mg mL⁻¹ H-MnO₂ under dark conditions overnight. Drugs can be loaded onto the carrier through the micropores on the surface of H-MnO₂. After centrifugation, the absorbance of supernatant at drug characteristic wavelength was determined by spectrophotometry. It is found by calculation that, at the feeding weight ratio (Drug: MnO₂) of 1:2, the loading ratio (Fig. 2c) of Ce6 and MTZ was evaluated to be 39.05% and 43.75%. And at the feeding weight ratio (drug:MnO₂) of 1:1, the loading ratio of Ce6 and MTZ was

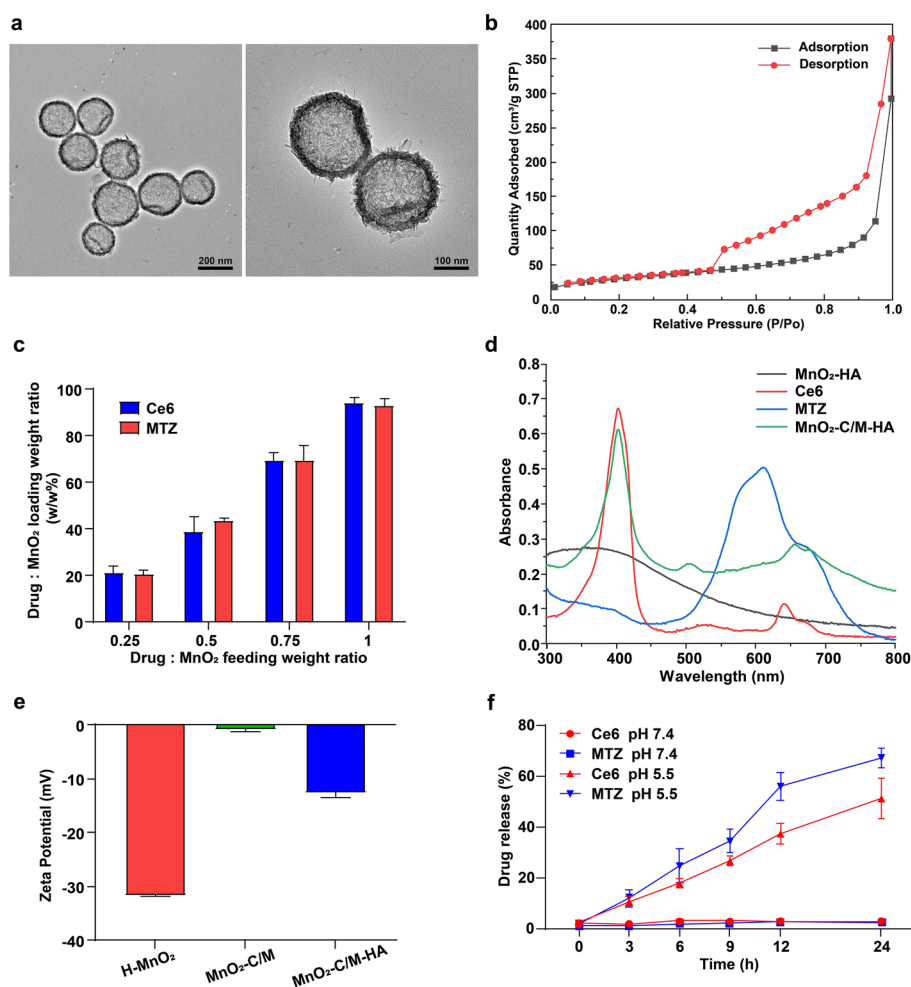


Fig. 2 Synthesis and characterization of MnO₂-C/M-HA. **a** TEM image of H-MnO₂ nanoparticles. **b** N₂ adsorption/desorption isotherms of the H-MnO₂ nanoparticles. **c** Ce6 and MTZ loading ratios in MnO₂ at different feeding drug: MnO₂ ratios. **d** The UV-Vis absorption spectra of Ce6, MTZ, MnO₂-HA and MnO₂-C/M-HA. **e** Zeta potential of H-MnO₂, MnO₂-C/M and MnO₂-C/M-HA, and data were expressed as mean ± SD (*n* = 3). **f** Percentages of released Ce6 and MTZ from MnO₂-C/M-HA over time under different conditions. Data were expressed as mean ± SD (*n* = 3)

evaluated to be 93.99% and 93.18%. The UV-Vis absorption spectra (Fig. 2d) of Ce6, MTZ, MnO₂-HA and MnO₂-C/M-HA can also confirm the successfully loading of Ce6 and MTZ. Due to the loading of two drugs, the absorption peaks of the nanomaterials at 400 nm and in the range of 600–700 nm have changed. The UV absorption spectra for samples loaded with only one drug in Additional file 1: Fig. S2 can be used as a reference too. By comparing the changes in Zeta potential (Fig. 2e) of H-MnO₂, MnO₂-C/M and MnO₂-C/M-HA can also demonstrate the successful drug loading and package of HA. With surface HA coating, it is obvious that the stability and dispersion (Additional file 1: Fig. S3) of MnO₂-C/M-HA were also improved.

According to TEM results in Additional file 1: Fig. S4, MnO₂ can be locally cleaved into Mn²⁺ under acidic conditions. To validate drug release (Fig. 2f), the MnO₂-C/M-HA were studied in solutions at different pH values. When the pH is 7.4, the nanomaterials

were very stable and few drugs were released. Compared with pH 7.4, the release speeds of drugs were much faster in mild acidic solutions. The release rate of MTZ reached 67.09% under the condition of pH 5.5 at 24 h. And the release rate of Ce6 is 51.21%. Thus, through the verification of the morphology and structure, drug loading properties and drug release efficiency of H-MnO₂, we proved that H-MnO₂ can be used as an effective carrier for MTZ and Ce6 combined delivery.

Photothermal properties of MnO₂-C/M-HA

Considering the NIR absorption of MnO₂-C/M-HA at about 660 nm, the photothermal properties of MnO₂-C/M-HA was studied. As presented in Fig. 3a, b, the temperature of MnO₂-C/M-HA of different concentrations (20, 40, 60, 80 and 100 µg mL⁻¹) were measured by infrared thermal imager every 60 s within 15 min. The temperature of MnO₂-C/M-HA solutions with a concentration of 100 µg mL⁻¹ could be raised to 55.5 °C under laser irradiation (660 nm, 1.0 W cm⁻²). In addition, the temperature of the MnO₂-C/M-HA solutions of 100 µg mL⁻¹ also increased along with the increase of irradiation power (0.6, 0.7, 0.8, 0.9 and 1.0 W cm⁻²) (Fig. 3c). The higher the power selected, the more obvious the temperature rose. To further prove the major heating components, as illustrated in Fig. 3d, MTZ is the most effective photothermal agent that can heat up in MnO₂-C/M-HA nanomaterials compared to other components such as MnO₂ and Ce6. By turning laser on and off, temperature changes of 100 µg mL⁻¹ MnO₂-C/M-HA

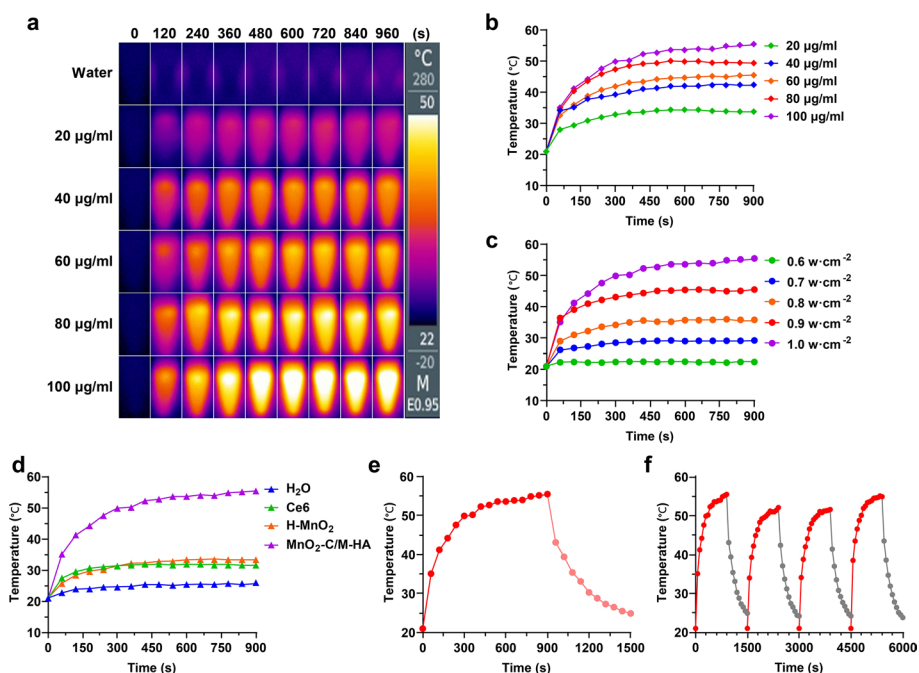


Fig. 3 Photothermal properties of MnO₂-C/M-HA. **a** Infrared thermal image of MnO₂-C/M-HA with different concentrations and under different irradiation time of the 660 nm laser (1.0 W cm⁻²). **b** Photothermal heating curves of MnO₂-C/M-HA with different concentrations under NIR laser (660 nm, 1.0 W cm⁻²). **c** Photothermal heating curves of MnO₂-C/M-HA (100 µg mL⁻¹) exposed to 660 nm laser with different power densities. **d** Photothermal heating curves of H₂O, Ce6, H-MnO₂ and MnO₂-C/M-HA under 660 nm laser irradiation (1.0 W cm⁻²). **e** Temperature variation curve of MnO₂-C/M-HA under 660 nm laser irradiation (1.0 W cm⁻²). **f** Temperature changes of MnO₂-C/M-HA during four on/off cycles of laser irradiation

were recorded (Fig. 3e) and the photothermal stability of MnO₂-C/M-HA was also tested under four cycles of heating and natural cooling (Fig. 3f). It was found that the photothermal effect of nanomaterials remained basically steady. The above experiments explained the MnO₂-C/M-HA could be used as a kind of stable nanodrug with excellent photothermal stability to ensure sustained photothermal tumor cell killing.

Cytotoxicity of MnO₂-C/M-HA in vitro

Before evaluating the effect of MnO₂-C/M-HA on 4T1 tumor cells, the uptake of nanomaterials by 4T1 cells was observed. The cell uptake of free Ce6 and MnO₂-Ce6-HA at different time points was observed by cellular imaging system (Additional file 1: Fig. S5). The results showed that the uptake of MnO₂-Ce6-HA by 4T1 cells was significantly higher than that of free Ce6. This suggests that drug delivery through H-MnO₂ and the inclusion of HA in the outer layer can increase drug uptake by 4T1 cells. Then, MTS assay was used to determine the effects of different drug treatment groups on 4T1 cytotoxicity at the same concentration for 24 h. Unmodified H-MnO₂ itself had less toxic effects on 4T1 cells. The cytotoxicity of nanomaterials was greatly enhanced after drug loading, and the killing effect was enhanced under the irradiation of 660 nm laser (Additional file 1: Figs. S6–S8). As shown in Fig. 4a, when treated with MnO₂-HA loaded with only one drug, it could have a certain degree of inhibition of cell activity compared with no drug loading. However, when MnO₂-HA was simultaneously loaded with MTZ and Ce6, the cell activity can be significantly inhibited under laser irradiation. The cell viability after MnO₂-C/M-HA with laser irradiation treatment was only 31.32%. This indicated that laser irradiation can simultaneously activate the PTT of MTZ and the PDT of Ce6. PTT and PDT, together with the chemotherapy effect of MTZ itself, synergistically inhibited the viability of 4T1 cells. In addition, we also used CoCl₂ to simulated cell hypoxia. According to Additional file 1: Fig. S9, the killing effect of MnO₂-C/M-HA with laser irradiation on 4T1 cells was still very obvious under the condition of hypoxia. The cell viability was only 52.16%. This suggested that the effect of MnO₂-C/M-HA nanomaterials was not affected by the hypoxic environment. It was mainly due to the oxygen provided by MnO₂. To further compare the cell activity and cytotoxicity of different treatment groups, cell live and dead assay was performed by Calcein-AM and PI double-fluorescence staining (Fig. 4b). YF[®]488-Annexin V and PI were also used to stain cells, and the apoptotic populations of the 4T1 cells treated with different formulations were analyzed and compared by flow cytometry (Fig. 4c). The quantitative results are shown in Fig. 4d. Compared with other treatment groups, MnO₂-C/M-HA with laser irradiation could hardly induce cell apoptosis. The apoptosis rate of the cells under this treatment could reach 96.81% on average.

In order to further verify the effect of PDT and ROS generation, we added DCFH-DA probe (Han et al. 2020; Wang et al. 2020a, b) to the treated cells and observed the production of ROS by fluorescence microscope (Fig. 4e). Under normoxia conditions, cells treated with Ce6, MnO₂-Ce6-HA and MnO₂-C/M-HA could produce ROS after laser irradiation, and the treatment groups with MnO₂ providing oxygen to Ce6 could produce more ROS. In the hypoxic condition, only adding Ce6 and laser irradiation produced insufficient ROS, but the MnO₂-Ce6-HA and the MnO₂-C/M-HA treatment groups could produce more ROS after laser irradiation (Additional file 1: Fig. S10).

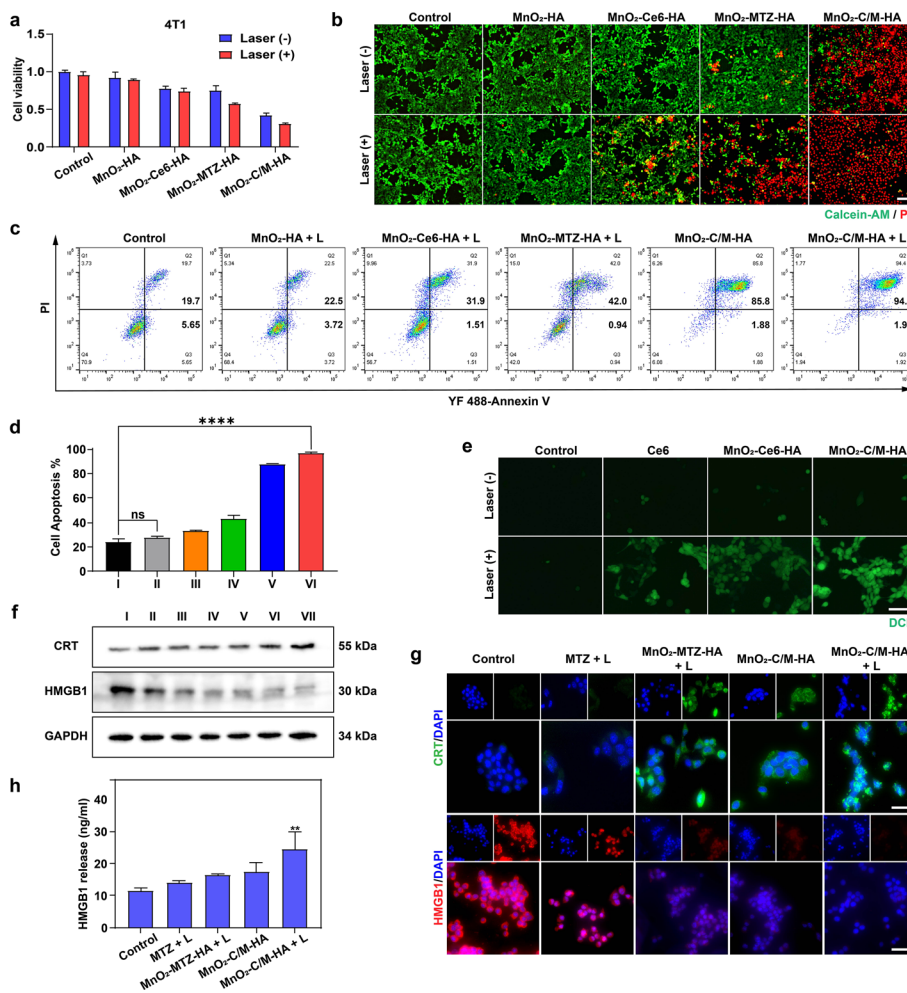


Fig. 4 In vitro experiments with MnO₂-C/M-HA. **a** The cytotoxicity of 4T1 cells of varying formulations with or without 660 nm (1.0 W cm⁻², 15 min) for 24 h. **b** Fluorescence images of Calcein-AM and PI double stained 4T1 cells treated by different formulations. Scale bar: 100 μm. **c** Flow cytometric analysis of apoptosis of 4T1 cells receiving different treatments and evaluated by Annexin V and PI staining. **d** Quantification results of apoptotic cells. I, Control; II, MnO₂-HA + laser; III, MnO₂-Ce6-HA + laser; IV, MnO₂-MTZ-HA + laser; V, MnO₂-C/M-HA; VI, MnO₂-C/M-HA + laser. **e** Fluorescence microscope images of ROS generation by DCFH-DA staining in cells. Scale bar: 100 μm. **f** Western blot analysis of CRT, HMGB1 proteins expression after 4T1 cells treated with different approaches. I, Control; II, MTZ; III, MnO₂-MTZ-HA; IV, MnO₂-C/M-HA; V, MTZ + laser; VI, MnO₂-MTZ-HA + laser; VII, MnO₂-C/M-HA + laser. **g** Fluorescence microscopic images to show the CRT exposure on and HMGB1 release from 4T1 cells after various treatments. Scale bar: 50 μm. **h** Detection of the released HMGB1. All the data were displayed as mean ± SD (*p < 0.05, **p < 0.01 and ****p < 0.0001)

Taken together, these results demonstrated that PDT, PTT and chemotherapy had been combined to achieve a significant effect on 4T1 cells by using MnO₂ as a carrier and providing oxygen.

ICD response of MnO₂-C/M-HA in vitro

MTZ itself can act as the inducer of ICD. PDT and PTT can also cause ICD. When ICD occurs, CRT expression is increased on the surface of tumor cells, sending a “eat me” signal to immune cells, which activates the immune response. HMGB1 itself is a protein highly expressed in the nucleus of tumor cells. When tumor cells

are stimulated, HMGB1 passes through the nuclear membrane and plasma membrane, migrates and releases into the extracellular cell, and activates the corresponding immune pathway (Krysko et al. 2012; Fucikova et al. 2020). As displayed in Fig. 4f, CRT and HMGB1 proteins expression after 4T1 cells treated with different drugs were assessed by western blot. Among different treatment groups, the expression of CRT proteins in the MnO₂-C/M-HA with laser treatment group was significantly higher than that in the other groups, while the content of HMGB1 was lower than that in the other groups. In addition, as shown in Fig. 4g, after 4T1 cells were treated with MnO₂-C/M-HA with laser irradiation, the expression of CRT proteins on cell membrane was particularly obviously. However, the expression of HMGB1 proteins in the nucleus were decreased compared with the control group, indicating that HMGB1 protein was released from the cell after drug stimulation. Besides, cell culture supernatants of different treatment groups were collected for ELISA, and the results showed that the release level of HMGB1 in MnO₂-C/M-HA with laser irradiation experimental group was the highest (Fig. 4h). These results indicated that MTZ itself, as well as the synergistic effect of PTT and PDT, induced ICD as expected. The induction effect of multiple combinations was stronger than that of single therapy. What's more, Mn²⁺ provided by MnO₂ also played an auxiliary role in the activation of immunity (Liang et al. 2018; Ding et al. 2020).

In the process of ICD, in addition to the role of CRT and HMGB1 in recruiting antigen presenting cells, ATP can also be released in an autophagy-dependent manner to send a “find me” signal to DC precursor cells and promote the clearance of tumor cells by immune cells (Krysko et al. 2012; Fucikova et al. 2020). In addition, when tumor cells undergo apoptosis or are in a toxic state, the intracellular ATP level will also decrease. According to the results shown in Additional file 1: Fig. S11, when MnO₂-C/M-HA and laser were used to treat 4T1 cells, the content of ATP in 4T1 cells was significantly reduced. These results indicated that the level of ATP in 4T1 cells decreased after being stimulated by nanodrugs, and ATP was induced to be released outside cell. Moreover, the induction effect of MnO₂-C/M-HA plus light is stronger than that of other treatment groups, which fully proves the multiple stimulation advantages and good application effect of MnO₂-C/M-HA nanomaterials.

In order to further verify the activation effect of DAMPs released by tumor cells on BMDCs in vitro during ICD (Liang et al. 2018), we conducted three-dimensional co-culture of 4T1 cells and BMDCs by non-contact communication cell chip (Additional file 1: Figs. S12 and S13). After mixing the matrix glue with the culture medium containing cells in equal proportion, 4T1 cells and BMDCs were inoculated at both ends of the chip, respectively, for 3D non-contact co-culture of cells (Fang et al. 2021). 4T1 cells were inoculated with MnO₂-C/M-HA and irradiated with laser to stimulate tumor cells to release DAMPs, which reached the end of BMDCs through the channel, thus stimulating the maturation of BMDCs. According to the immunofluorescence results of the expression of DC maturity markers CD80 and CD86 in Additional file 1: Figs. S14 and S15, the maturity of BMDCs after 4T1 cells were stimulated with MnO₂-C/M-HA with laser irradiation was more obvious than that of the PBS group, indicating that this kind of nano-drugs could induce ICD well and stimulated DCs maturation as expected in vitro.

In vitro studies, we verified the cytotoxicity and apoptosis inducing effect of MnO₂-C/M-HA on 4T1 tumor cells. Next, the CRT, HMGB1 and ATP expressed or released by tumor cells after stimulation were detected, which proved that MnO₂-C/M-HA could synergically enhance ICD. Finally, the activation of DCs in vitro was verified, providing sufficient data support for subsequent anti-tumor immunotherapy in mice.

Antitumor efficiency of MnO₂-C/M-HA in 4T1 tumor-bearing BALB/c mice

The in vivo anti-tumor efficacy of MnO₂-C/M-HA was examined in 4T1 tumor-bearing BALB/c female mice. The treatment schedule is shown in Fig. 5a. Specifically, BALB/c female mice were randomly divided into seven groups on the seventh

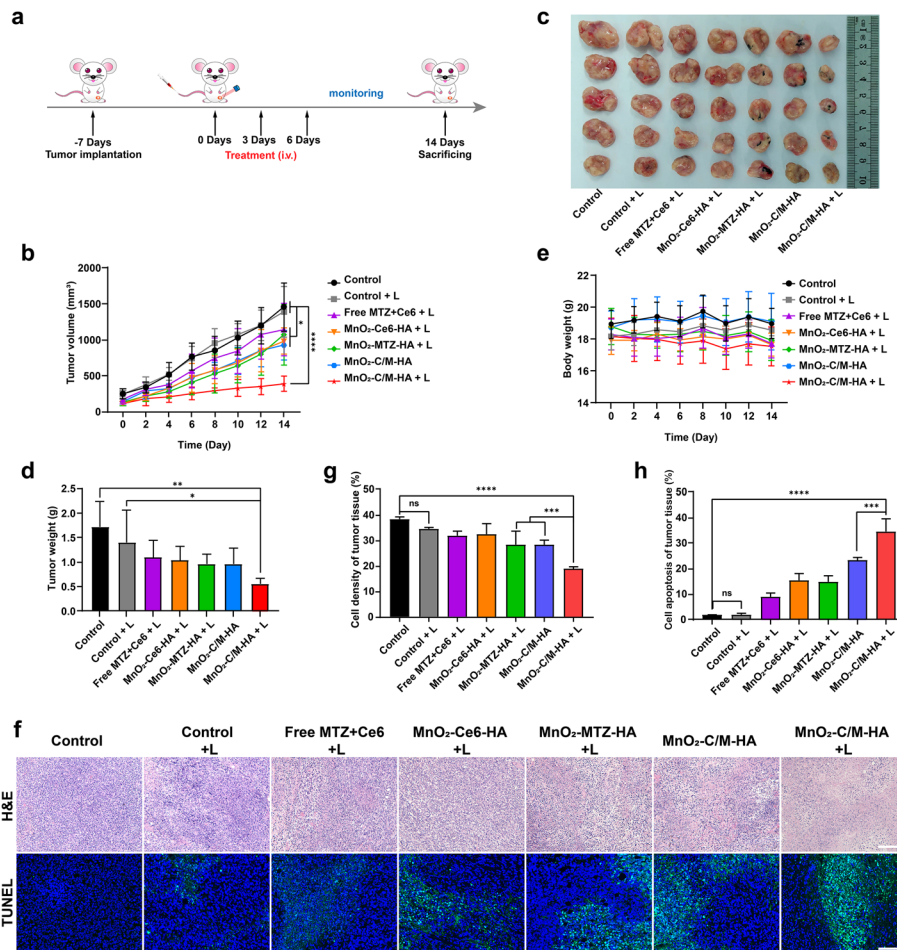


Fig. 5 Antitumor efficiency of MnO₂-C/M-HA in 4T1 tumor-bearing BALB/c mice. **a** Schematic illustration of treatment schedule for 4T1 tumor-bearing BALB/c mice. **b** Tumor growth curves of different groups during the therapeutic course of 14 days. **c** Photographs of excised solid tumors at the end of anti-tumor studies. **d** Tumor weights of different groups at the endpoints of treatment schedule. **e** Body weight changes of 4T1 tumor-bearing BALB/c mice of different groups during the treatment. **f** Histopathological analysis: immunohistochemical or immunofluorescence staining of the sections from excised tumors on day 14 in terms of H&E and TUNEL. Scale bars: 100 μm for H&E and 200 μm for TUNEL. **g-h** Semi-quantitative statistical analysis of H&E staining and TUNEL staining of tumor tissue slices. All the data were displayed as mean ± SD (**p* < 0.05, ***p* < 0.01 and *****p* < 0.0001)

day after 4T1 tumor cell inoculation on breast pad to give different treatments. The laser (660 nm, 1.0 W cm^{-2} for 5 min) was applied 12 h after intravenous injection with different drugs. In order to ensure that the drug can successfully reach the tumor site after intravenous injection, fluorescent imaging of the main organs and tissue was performed 12 h after administration (Additional file 1: Fig. S16). By detecting the fluorescence of Ce6 (Phua et al. 2019; Han et al. 2020; Liu et al. 2021a, b), it was observed that the drug could reach the tumor site smoothly.

The body weight and tumor volume were monitored regularly during the treatment. As shown in Fig. 5b, the mice in control group and control with laser group showed rapid growth in tumor volume. In contrast, the increase in tumor size was significantly inhibited in the $\text{MnO}_2\text{-C/M-HA}$ with laser irradiation group. Figure 5c shows the photos of the solid tumors removed after the treatment, and the actual tumor size of each group was consistent with the changes in tumor volume measured above. Moreover, the tumor weight also exhibited the same tendencies in different groups (Fig. 5d). The body weights of mice had no obvious changes during the 14 days of treatment (Fig. 5e). Besides, at the end of the anti-tumor study, the hematoxylin and eosin (H&E) staining of the main organs also showed no difference from normal (Additional file 1: Fig. S17), indicating that the drug had little influence on the normal growth of mice.

We also tested the hemolytic reaction of $\text{MnO}_2\text{-C/M-HA}$ as shown in Additional file 1: Fig. S18. Compared with the positive control group (water and red blood cells), it was found that $\text{MnO}_2\text{-HA}$ and $\text{MnO}_2\text{-C/M-HA}$ had a very low hemolysis rate and good blood compatibility. Besides, we evaluated the in vivo toxicology of $\text{MnO}_2\text{-C/M-HA}$. $\text{MnO}_2\text{-C/M-HA}$ was intravenously injected into healthy female Balb/c mice. Blood samples were collected at 1, 4 and 7 days after administration. Levels of liver function markers such as alanine aminotransferase (ALT), alkaline phosphatase (ALP) and aspartate aminotransferase (AST), as well as creatinine (CREA), blood urea nitrogen (BUN) and total blood protein (TP) were tested. As shown in Additional file 1: Fig. S19, we found that the indexes of mice were within the normal range, indicating that $\text{MnO}_2\text{-C/M-HA}$ did not cause significant liver and kidney damage. It had low toxic side effects.

For tumor tissue, H&E staining and immunofluorescence staining of TUNEL (cell apoptosis marker) (Fig. 5f) showed the largest damaged area in tumor tissues and a significant increase in cell apoptosis after treatment with $\text{MnO}_2\text{-C/M-HA}$ with laser irradiation. The other groups with incomplete treatment had relatively moderate damage to tumor tissue. And Additional file 1: Fig. S20 shows the whole tumor staining of TUNEL. Based on the H&E staining results, the cell density of tumor tissues was analyzed semi-quantitatively. According to the results in Fig. 5g, it can also be found that after $\text{MnO}_2\text{-C/M-HA}$ combined with light treatment, the cell density of tumor tissue was significantly reduced. The cell density of tumor tissues in $\text{MnO}_2\text{-C/M-HA}$ with laser irradiation group was only 19.15%. Combined with TUNEL fluorescence staining of tumor tissue slices, we performed semi-quantitative analysis of apoptotic area in tumor tissue. According to the results in Fig. 5h, we can also find that in the group treated with $\text{MnO}_2\text{-C/M-HA}$ plus light, the proportion of apoptosis occurred in tumor tissues was the highest. It could reach 34.52% on average, 18.76 times that of the control group.

Immune response induced by MnO₂-C/M-HA in vivo

In order to ensure the immunotherapy effect of MnO₂-C/M-HA, we also verified the in vivo photothermal effect of MnO₂-C/M-HA during the treatment (Fig. 6a, b). As monitored by infrared thermal camera under laser irradiation (660 nm, 1.0 W cm⁻²), the surface temperature of the tumor injected with MnO₂-C/M-HA increased to 54.2 °C. To test the effect of ICD in vivo, we collected tumors on the 14th day of treatment to verify the expression of CRT and HMGB1 protein in tumor tissues by western blot (Fig. 6c). Combined with the results of immunohistochemical staining (Additional file 1: Fig. S21), we found that the treatment of MnO₂-C/M-HA with laser irradiation remarkably promoted the expression of CRT and the release of HMGB1. The expression or release of these two proteins was relatively insufficient in other treatment groups. To further clarify the immune response of MnO₂-C/M-HA induced ICD, we analyzed the infiltrating immune cells at the tumor site by flow cytometry. Initially, we analyzed the DC maturation in the tumor (Fig. 6d and Additional file 1: Fig. S22). The results showed that DCs

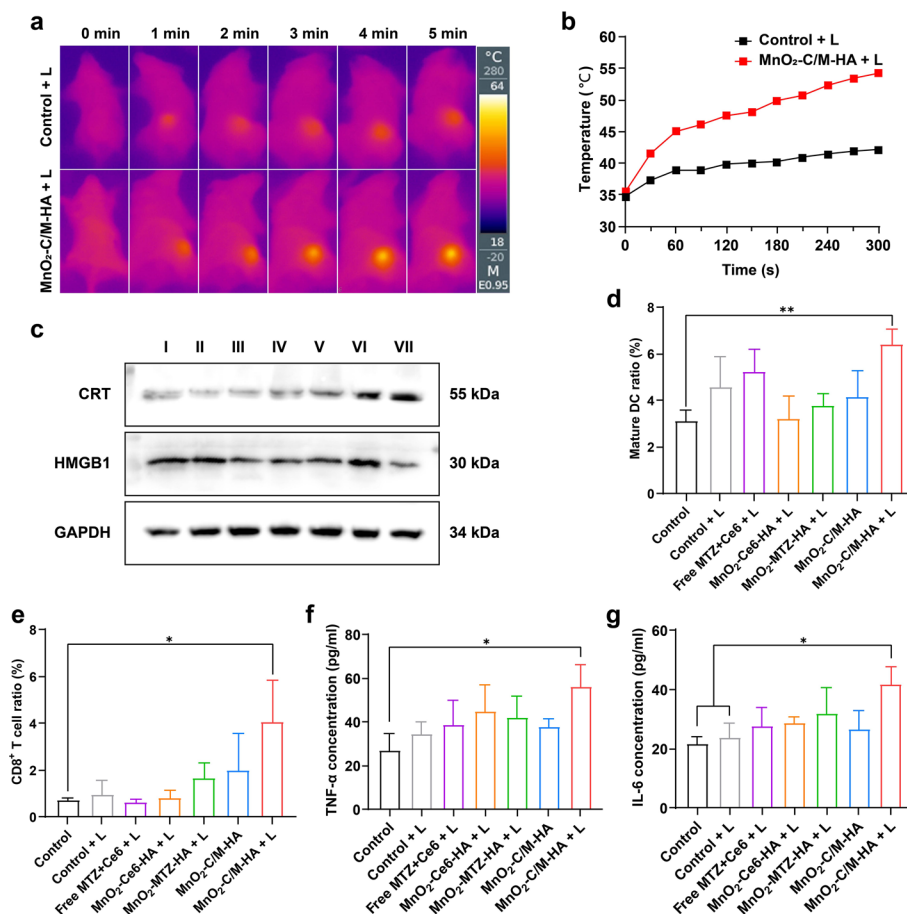


Fig. 6 Immune response induced by MnO₂-C/M-HA in vivo. **a** Photothermal images of tumor-bearing mice model. **b** The temperature changing curves of photothermal imaging in tumor site under laser treatment (660 nm, 1.0 W cm⁻², 5 min). **c** Western blot results of CRT and HMGB1 expression in tumor tissues. I, Control; II, Control + laser; III, Free MTZ + Ce6 + laser; IV, MnO₂-Ce6-HA + laser; V, MnO₂-MTZ-HA + laser; VI, MnO₂-C/M-HA; VII, MnO₂-C/M-HA + laser. **d-e** Flow cytometry examined DC maturation levels and CD8⁺ CD8⁺ T cells in the tumor tissue of mice. **f-g** ELISA results of the level of the secreted TNF- α and IL-6 in blood serum after various treatments. All the data were displayed as mean \pm SD (* p < 0.05, ** p < 0.01 and *** p < 0.001)

maturity was the highest in MnO₂-C/M-HA with laser treatment group which could reach 6.43% averagely about 2.07 times of the control group. It indicates that DMAPs released by tumor cells successfully recruited DCs cells and effectively stimulated the maturation of DCs after drug stimulation. Mature DCs are associated with antigen presentation, thereby activating the anti-tumor effects of T cells (Jia et al. 2020; Zhou et al. 2021). Next, we analyzed the infiltration of T lymphocytes in the tumor by flow cytometry (Fig. 6e and Additional file 1: Fig. S23). It suggested that the MnO₂-C/M-HA with laser irradiation group recruited more infiltrating CD8⁺ T cells which reached 4.08% averagely. It was about 5.67 times higher than the control group. This indicates that the adaptive immune response can be successfully induced in mice after the stimulation of MnO₂-C/M-HA photoactivated nanomaterials.

Elevated levels of pro-inflammatory cytokines are also a criterion for successful induction of ICD (Jia et al. 2020; Jiao et al. 2021; Lu et al. 2021). To this end, we detected the expression of pro-inflammatory cytokines TNF- α and IL-6 in serum of mice in different treatment groups by ELISA (Fig. 6f, g). Compared with other control groups, the levels of TNF- α and IL-6 in serum of mice treated with MnO₂-C/M-HA with laser irradiation were significantly increased. Concretely reflected in that, the average concentration of TNF- α and IL-6 in the MnO₂-C/M-HA with laser irradiation group reached 56.33 pg mL⁻¹ and 41.73 pg mL⁻¹, respectively. While the control group only reached 26.81 pg mL⁻¹ and 21.66 pg mL⁻¹. All in all, we evaluated the anti-tumor and immune effect of MnO₂-C/M-HA in vivo, demonstrating that the combination of chemotherapy, PTT, PDT and MnO₂ nanoplatform can better induce ICD and play the strongest role in inhibiting primary breast cancer. And the good applicability of this nanodrug is proved by biosafety evaluation.

Conclusions

In summary, an acid-responsive MnO₂-C/M-HA multifunctional nanomaterial was successfully developed. Using the hollow structure of H-MnO₂ nanometer carriers, we successfully realized the simultaneous payload of different kinds of drugs. And the uptake of drugs by tumor cells also increased significantly. ROS production during PDT can be increased by using oxygen produced by MnO₂ degrade in an acidic environment. The effect of phototherapy was obviously enhanced. By loading Ce6 and MTZ, PDT/PTT can be combined with chemotherapy to enhance the induction effect of ICD. In anti-tumor therapy, this kind of nanomaterials can effectively stimulate the maturation of DCs, increase the infiltration of cytotoxic CD8⁺ T lymphocytes, and induce systemic anti-tumor immune response. Thus, the growth of primary tumors was greatly inhibited and the damage and necrosis of tumor tissues were induced. This not only makes up for the limitations of monotherapy in anti-tumor immunity, but also provides a multifunctional immunotherapy nanoplatform for tumor therapy.

Supplementary Information

The online version contains supplementary material available at <https://doi.org/10.1186/s12645-023-00173-y>.

Additional file 1. Figure S1. Synthesis process of hollow MnO₂. **Figure S2.** UV-vis-NIR spectra of MnO₂-Ce6-HA and MnO₂-MTZ-HA. **Figure S3.** Physiological stability evaluation: Digital images of H-MnO₂ and MnO₂-C/M-HA dispersed in H₂O, PBS and DMEM solution for 24 h. **Figure S4.** TEM image of H-MnO₂ at pH 7.4 and pH 5.5. **Figure S5.** Fluorescence microscopic images of 4T1 cells incubated with Free Ce6 or MnO₂-Ce6-HA at different time points.

Scale bar: 50 μm . **Figure S6.** Cell viability of 4T1 with different concentrations of MTZ with or without 660 nm (1.0 W-cm⁻², 15 min) for 24 h. **Figure S7.** Cell viability of 4T1 with different concentrations of MnO₂-HA for 24 h. **Figure S8.** Cell viability of 4T1 with different concentrations of MnO₂-C/M-HA with or without 660 nm (1.0 W-cm⁻², 15 min) for 24 h. **Figure S9.** The cytotoxicity of 4T1 cells of varying formulations with or without 660 nm (1.0 W-cm⁻², 15 min) for 24 h in hypoxia. **Figure S10.** Fluorescence microscope images of ROS generation by DCFH-DA staining in cells in hypoxia. Scale bar: 100 μm . **Figure S11.** Intracellular ATP level after various treatments. **Figure S12.** Schematic diagram of co-culture by non-contact communication cell chip. **Figure S13.** Local structure of non-contact communication cell chip. **Figure S15.** Immunofluorescence of CD11c in 3D-cell cultures of BMDCs. Scale bar: 50 μm . **Figure S15.** Immunofluorescence of CD80/CD86 in 3D-cell cultures of BMDCs. Scale bar: 50 μm . **Figure S16.** Ex vivo fluorescence images (12 h post-injection) of 4T1 tumor-bearing mice organs or tissue treated with free Ce6 and MnO₂-C/M-HA. **Figure S17.** H&E staining of heart, liver, spleen, lung, and kidney at the end of antitumor study. Scale bar: 100 μm . **Figure S18.** Hemolysis rate by incubating RBCs with MnO₂-HA and MnO₂-C/M-HA at different concentrations (25–100 $\mu\text{g}/\text{mL}$) for 4 h. **Figure S19.** Blood biochemical indices of healthy mice at day 1, 4 and 7 after intravenous injection of MnO₂-C/M-HA. **Figure S20.** The whole tumor staining of TUNEL. Scale bar: 1000 μm . **Figure S21.** Immunohistochemical assay of CRT and HMGB1 in the tumor tissues after various treatments. Scale bar: 200 μm . **Figure S22.** Representative flow cytometry plots showing mature DCs (CD11c+CD80+CD86+) after various treatments. **Figure S23.** Representative flow cytometry plots showing cytotoxic T lymphocytes (CD3+CD8+) after various treatments. **Table S1.** Antibodies were used for WB, FC or IF/IHC in this study.

Acknowledgements

The authors gratefully acknowledge the Nanjing University of Chinese Medicine.

Author contributions

YW and RW contributed equally to this work. YW, RW, PS, WZ, and KY performed the in vivo experiments. YW, CC, and JY performed materials characterization. YW and RW wrote the manuscript with feedback from all the authors. XG, XH, and YS conceived the idea, designed the experiments and supervised the project. All authors read and approved the final manuscript.

Funding

This work was supported by a Key International Cooperation of the National Natural Science Foundation of China (81920108029 and 31901010), the Key Foundation for Social Development Project of the Jiangsu Province of China (BE2021741), Jiangsu Specially Appointed Professorship Foundation Practice Innovation Program of Jiangsu Province (KYCX22_1969), the Priority Academic Program Development of Jiangsu Higher Education Institutions (Integration of Chinese and Western Medicine). The authors would like to thank the experiment center for science and technology, Nanjing University of Chinese Medicine for providing instrumental assistance.

Data Availability

All data generated or analyzed during this study are included in this published article and its supplementary information files.

Declarations

Ethics approval and consent to participate

Not applicable.

Consent for publication

All authors consent for publication.

Competing interests

The authors declare no competing interests.

Received: 21 November 2022 Accepted: 5 March 2023

Published online: 11 March 2023

References

- Agostinis P, Berg K, Cengel KA, Foster TH, Girotti AW, Gollnick SO, Hahn SM, Hamblin MR, Juzeniene A, Kessel D, Korbelik M, Moan J, Mroz P, Nowis D, Piette J, Wilson BC, Golab J (2011) Photodynamic therapy of cancer: an update. *CA Cancer J Clin* 61(4):250–281
- Alzeibak R, Mishchenko TA, Shilyagina NY, Balalaeva IV, Vedunova MV, Kryskov DV (2021) Targeting immunogenic cancer cell death by photodynamic therapy: past, present and future. *J Immunother Cancer* 9(1):1
- Boedtker E, Pedersen SF (2020) The acidic tumor microenvironment as a driver of cancer. *Annu Rev Physiol* 82:103–126
- Bol KF, Schreibelt G, Gerritsen WR, de Vries IJ, Figdor CG (2016) Dendritic cell-based immunotherapy: state of the art and beyond. *Clin Cancer Res* 22(8):1897–1906
- Cao W, Liu B, Xia F, Duan M, Hong Y, Niu J, Wang L, Liu Y, Li C, Cui D (2020) MnO₂@Ce6-loaded mesenchymal stem cells as an “oxygen-laden guided-missile” for the enhanced photodynamic therapy on lung cancer. *Nanoscale* 12(5):3090–3102

- Dai Z, Tang J, Gu Z, Wang Y, Yang Y, Yang Y, Yu C (2020) Eliciting immunogenic cell death via a unitized nanoinducer. *Nano Lett* 20(9):6246–6254
- Deng X, Shao Z, Zhao Y (2021) Solutions to the drawbacks of photothermal and photodynamic cancer therapy. *Adv Sci (weinh)* 8(3):2002504
- Ding B, Zheng P, Jiang F, Zhao Y, Wang M, Chang M, Ma P, Lin J (2020) MnO_x nanospikes as nanoadjuvants and immunogenic cell death drugs with enhanced antitumor immunity and antimetastatic effect. *Angew Chem Int Ed Engl* 59(38):16381–16384
- Donohoe C, Senge MO, Arnaut LG, Gomes-da-Silva LC (2019) Cell death in photodynamic therapy: from oxidative stress to anti-tumor immunity. *Biochim Biophys Acta Rev Cancer* 1872(2):188308
- Fan Y, Kuai R, Xu Y, Ochyl LJ, Irvine DJ, Moon JJ (2017) Immunogenic cell death amplified by co-localized adjuvant delivery for cancer immunotherapy. *Nano Lett* 17(12):7387–7393
- Fang G, Lu H, Aboukheyr Es H, Wang D, Liu Y, Warkiani ME, Lin G, Jin D (2021) Unidirectional intercellular communication on a microfluidic chip. *Biosens Bioelectron* 175:112833
- Fucikova J, Kepp O, Kasikova L, Petroni G, Yamazaki T, Liu P, Zhao L, Spisek R, Kroemer G, Galluzzi L (2020) Detection of immunogenic cell death and its relevance for cancer therapy. *Cell Death Dis* 11(11):1013
- Garg AD, Agostinis P (2017) Cell death and immunity in cancer: from danger signals to mimicry of pathogen defense responses. *Immunol Rev* 280(1):126–148
- Han L, Wang Y, Huang X, Liu F, Ma C, Feng F, Zhang J, Liu W, Qu W, Pang H, Xue J (2020) Specific-oxygen-supply functionalized core-shell nanoparticles for smart mutual-promotion between photodynamic therapy and gambogic acid-induced chemotherapy. *Biomaterials* 257:120228
- Huang J, Huang Y, Xue Z, Zeng S (2020) Tumor microenvironment responsive hollow mesoporous Co9S8@MnO₂-ICG/DOX intelligent nanoplatfor for synergistically enhanced tumor multimodal therapy. *Biomaterials* 262:120346
- Jeong H, Park W, Kim DH, Na K (2021) Dynamic nanoassemblies of nanomaterials for cancer photomedicine. *Adv Drug Deliv Rev* 177:113954
- Jia L, Pang M, Fan M, Tan X, Wang Y, Huang M, Liu Y, Wang Q, Zhu Y, Yang X (2020) A pH-responsive Pickering nanoe-mulsion for specified spatial delivery of immune checkpoint inhibitor and chemotherapy agent to tumors. *Theranostics* 10(22):9956–9969
- Jiao X, Sun L, Zhang W, Ren J, Zhang L, Cao Y, Xu Z, Kang Y, Xue P (2021) Engineering oxygen-deficient ZrO₂-x nanoplatfor as therapy-activated “immunogenic cell death (ICD)” inducer to synergize photothermal-augmented sonodynamic tumor elimination in NIR-II biological window. *Biomaterials* 272:120787
- Kroemer G, Galluzzi L, Kepp O, Zitvogel L (2013) Immunogenic cell death in cancer therapy. *Annu Rev Immunol* 31:51–72
- Krysko DV, Garg AD, Kaczmarek A, Krysko O, Agostinis P, Vandenabeele P (2012) Immunogenic cell death and DAMPs in cancer therapy. *Nat Rev Cancer* 12(12):860–875
- Li W, Yang J, Luo L, Jiang M, Qin B, Yin H, Zhu C, Yuan X, Zhang J, Luo Z, Du Y, Li Q, Lou Y, Qiu Y, You J (2019) Targeting photodynamic and photothermal therapy to the endoplasmic reticulum enhances immunogenic cancer cell death. *Nat Commun* 10(1):3349
- Liang R, Liu L, He H, Chen Z, Han Z, Luo Z, Wu Z, Zheng M, Ma Y, Cai L (2018) Oxygen-boosted immunogenic photodynamic therapy with gold nanocages@manganese dioxide to inhibit tumor growth and metastases. *Biomaterials* 177:149–160
- Liu P, Zhou Y, Shi X, Yuan Y, Peng Y, Hua S, Luo Q, Ding J, Li Y, Zhou W (2021a) A cyclic nano-reactor achieving enhanced photodynamic tumor therapy by reversing multiple resistances. *J Nanobiotechnol* 19(1):149
- Liu Y, Zhou J, Li Q, Li L, Jia Y, Geng F, Zhou J, Yin T (2021b) Tumor microenvironment remodeling-based penetration strategies to amplify nanodrug accessibility to tumor parenchyma. *Adv Drug Deliv Rev* 172:80–103
- Lu Y, Xu F, Wang Y, Shi C, Sha Y, He G, Yao Q, Shao K, Sun W, Du J, Fan J, Peng X (2021) Cancer immunogenic cell death via photo-pyroptosis with light-sensitive Indoleamine 2,3-dioxygenase inhibitor conjugate. *Biomaterials* 278:121167
- Mei KC, Liao YP, Jiang J, Chiang M, Khazaieli M, Liu X, Wang X, Liu Q, Chang CH, Zhang X, Li J, Ji Y, Melano B, Telesca D, Xia T, Meng H, Nel AE (2020) Liposomal delivery of mitoxantrone and a cholesteryl indoximod prodrug provides effective chemo-immunotherapy in multiple solid tumors. *ACS Nano* 14(10):13343–13366
- Ni W, Wu J, Fang H, Feng Y, Hu Y, Lin L, Chen J, Chen F, Tian H (2021) Photothermal-chemotherapy enhancing tumor immunotherapy by multifunctional metal-organic framework based drug delivery system. *Nano Lett* 21(18):7796–7805
- Phua SZF, Yang G, Lim WQ, Verma A, Chen H, Thanabalu T, Zhao Y (2019) Catalase-integrated hyaluronic acid as nano-carriers for enhanced photodynamic therapy in solid tumor. *ACS Nano* 13(4):4742–4751
- Sabado RL, Balan S, Bhardwaj N (2017) Dendritic cell-based immunotherapy. *Cell Res* 27(1):74–95
- Sun Y, Zhao D, Wang G, Wang Y, Cao L, Sun J, Jiang Q, He Z (2020) Recent progress of hypoxia-modulated multifunctional nanomedicines to enhance photodynamic therapy: opportunities, challenges, and future development. *Acta Pharm Sin B* 10(8):1382–1396
- Wang M, Chang M, Chen Q, Wang D, Li C, Hou Z, Lin J, Jin D, Xing B (2020a) Au₂Pt-PEG-Ce6 nanoformulation with dual nanozyme activities for synergistic chemodynamic therapy/phototherapy. *Biomaterials* 252:120093
- Wang Y, Zhang J, Lv X, Wang L, Zhong Z, Yang DP, Si W, Zhang T, Dong X (2020b) Mitoxantrone as photothermal agents for ultrasound/fluorescence imaging-guided chemo-phototherapy enhanced by intratumoral H₂O₂-Induced CO. *Biomaterials* 252:120111
- Xu P, Liang F (2020) Nanomaterial-based tumor photothermal immunotherapy. *Int J Nanomed* 15:9159–9180
- Yang Y (2015) Cancer immunotherapy: harnessing the immune system to battle cancer. *J Clin Invest* 125(9):3335–3337
- Yang G, Xu L, Chao Y, Xu J, Sun X, Wu Y, Peng R, Liu Z (2017) Hollow MnO₂ as a tumor-microenvironment-responsive biodegradable nano-platfor for combination therapy favoring antitumor immune responses. *Nat Commun* 8(1):902

- Yu F, Shang X, Zhu Y, Lou H, Liu Y, Meng T, Hong Y, Yuan H, Hu F (2021) Self-preparation system using glucose oxidase-inspired nitroreductase amplification for cascade-responsive drug release and multidrug resistance reversion. *Biomaterials* 275:120927
- Zhang Y, Zhang Z (2020) The history and advances in cancer immunotherapy: understanding the characteristics of tumor-infiltrating immune cells and their therapeutic implications. *Cell Mol Immunol* 17(8):807–821
- Zhang X, Lu Y, Jia D, Qiu W, Ma X, Zhang X, Xu Z, Wen F (2021) Acidic microenvironment responsive polymeric MOF-based nanoparticles induce immunogenic cell death for combined cancer therapy. *J Nanobiotechnology* 19(1):455
- Zhou W, Zhou Y, Chen X, Ning T, Chen H, Guo Q, Zhang Y, Liu P, Zhang Y, Li C, Chu Y, Sun T, Jiang C (2021) Pancreatic cancer-targeting exosomes for enhancing immunotherapy and reprogramming tumor microenvironment. *Biomaterials* 268:120546
- Zou L, Wang H, He B, Zeng L, Tan T, Cao H, He X, Zhang Z, Guo S, Li Y (2016) Current approaches of photothermal therapy in treating cancer metastasis with nanotherapeutics. *Theranostics* 6(6):762–772

Publisher's Note

Springer Nature remains neutral with regard to jurisdictional claims in published maps and institutional affiliations.

Ready to submit your research? Choose BMC and benefit from:

- fast, convenient online submission
- thorough peer review by experienced researchers in your field
- rapid publication on acceptance
- support for research data, including large and complex data types
- gold Open Access which fosters wider collaboration and increased citations
- maximum visibility for your research: over 100M website views per year

At BMC, research is always in progress.

Learn more biomedcentral.com/submissions

